

Manufacturability and Mechanical Assessment of Ti-6Al-4V 3D Printed Structures for Patient-Specific Implants

Fatemeh Zarei^a, Aziz Shafiei-Zarghani^{b*}, Fatemeh Dehnavi^a

^a Department of Materials Science and Engineering, School of Materials and Civil Engineering, Shiraz University, Shiraz, IRAN.

^b Department of Materials Science and Engineering, School of Materials and Civil Engineering, Shiraz University, Shiraz, IRAN. Email: a3shafiei@gmail.com, ashafiei@shirazu.ac.ir

Acknowledgments

This work was supported by the Shiraz University and Mehrawin Shiraz Company. The Micro-Computed Tomography (Micro-CT) test machine used in this study was funded by the pre-clinical laboratory of Tehran University of Medical Sciences.

Abstract

Recent advances in additive manufacturing (3D printing) of metallic materials have opened new doors to the design and fabrication of geometrically patient-specific and mechanically tailored implants for bone tissue reconstruction. An architected internal structure for the implant with a unique design capable of tailoring the mechanical properties of the implant to be analogous to that of the injured bone could improve osseointegration by resolving the stress shielding issue. This work aims to propose a new, simple, fast, and clinically applicable approach for designing the trabecular-like structure of tailored implants, focusing on the tibia component in the knee joint replacement. The conceptual lattice structures with different solid fractions were designed and manufactured using the Selective Laser Melting (SLM) technique and Ti-6Al-4V alloy. The mechanical behavior of the structures was computationally and experimentally measured, evaluated, and compared with that of the natural tibia bone. Additionally, the geometrical accuracy of the printed structures is characterized using X-ray computed tomography and microscopic examinations to assess manufacturing robustness with regard to the original design intent. Results showed that the permeability of fabricated structures is between 0.16×10^{-9} and 0.38×10^{-9} , which is in the range of that of trabecular bones. In addition, the mechanical results indicated that the stiffness and strength of designed structures range from 1.08 to 4.47 GPa and 147 to 295 MPa, respectively, which are reasonably consistent with natural bone. Finally, a conceptual design framework indicating the isolated correlation between the solid fraction of the lattices and the expected biomechanical behavior is proposed.

Keywords: Patient-Specific Implant, Additive Manufacturing, Selective Laser Melting (SLM), Trabecular Bone, TPMS Structure

1. Introduction

Titanium (Ti) and its alloys are widely used in biomedical applications thanks to their specific set of properties such as great corrosion resistance, special biocompatibility, excellent mechanical properties including high specific strength and stiffness, and high fracture toughness. In this field of application, Ti6Al4V is the most used titanium alloy and is generally used in joint replacement owing to its unique fatigue resistance (Dhiman et al., 2021, 2019; Liu et al., 2020; Shah et al., 2016; Singh et al., 2020; Singla et al., 2021). However, it has a major drawback; its elastic modulus (110 GPa (Geetha et al., 2009)) is larger than that of human bone (that of cortical and trabecular bone ranging from 0.5 GPa to a maximum of 30 GPa (Katz, 1980; Ma et al., 2019)). This serious modulus mismatch can cause uneven load distribution at the interface of natural bone and implant, resulting in implant loosening or autogenous bone fracture (Krishna et al., 2007). This phenomenon is also known as “stress shielding”, and leads to the reduction of implant longevity (Aufa et al., 2022). Introducing micro-architected implants which possess lightweight lattice structures gave rise to this problem. The architecture of these structures is of great importance and their geometry, strut size, and solid fraction should be tailored since their characteristics not only affect the mechanical behavior of the implant, but also the cell attachment, cell growth, and transport of cellular nutrients and metabolites (Benedetti et al., 2021; Hsieh et al., 2021; van Blitterswijk et al., 1986). Therefore, a well-designed geometry can successfully prevent osteonecrosis and osteogenesis deformities around the implant.

Triply Periodic Minimal Surfaces (TPMS) that are known for the zero-mean curvature of their surfaces and high specific surface area which prepare a vast surface area for cell growth, have recently attracted a lot of attention as a versatile category of structures for use in micro-architected implants (Bidan et al., 2013; Jinnai et al., 2002). In addition to their geometrical features which derive benefits of cell growth and attachment, Bobbert et al (Bobbert et al., 2017) reported that these structures are capable of representing low stiffness with relatively high strength. One of the unique characteristics of TPMS structures is that their mechanical and biological properties can be adjusted like the injured bone only by controlling their

equations to modify parameters like the channel sizes. TPMS geometries possess different structures such as Schwartz Primitive, Schwartz Diamond, Gyroid, etc. However, it is not possible to say which structure has a superior behavior because each has its own special properties. As one of the greatest designed TPMS structures, the gyroid structure has shown terrific mechanical performance and also interesting self-supported features (Yan et al., 2014). Yu et al. (Yu et al., 2020) compared the compressive and tensile strength of primitive, gyroid, and bcc structures and reported that the gyroid had the finest mechanical behavior. Moreover, it represents good feasibility and accuracy of manufacturing. Barba and co-workers (Barba et al., 2019) addressed some points of different biomedical lattices by a conceptual methodology and concluded that the choice of lattice topology has a strong influence on the geometrical precision that can be achieved, and reported that Gyroid presents significant manufacturability and consequently superior mechanical behavior. Therefore, the TPMS structure that is selected for this work is gyroid. Due to the complex and periodic architecture of TPMS structures, their 3D production was not possible until the advent of 3D printing, although the study of their mathematical relationships had begun decades ago. Selective Laser Melting (SLM) is a renowned additive manufacturing method that utilizes a powder bed and a heat source to create 3D metal shapes with high dimensional accuracy. SLM enables the production of complex scaffolds with such an excellent quality that was impossible with conventional methods (Bertol et al., 2010; Mullen et al., 2009; Yuan et al., 2019).

Considering the importance of fabricating an implant with the same mechanical properties of the related injured bone, in the current work it was decided to design and evaluate the mechanical properties of different gyroid lattice structures with various solid fractions of 16, 26, 36 and 56. In addition, two groups of samples were fabricated with Ti6Al4V alloy and SLM machine in order to examine their manufacturability and mass-flow properties and also to validate the numerical assessments of mechanical behaviors. In brief, the main aim is to find a new and simple isolated relationship between the solid fraction (relative density) of the internal architecture of implants and their stiffness, strength, and energy absorption

properties. The proposed equations can be used as a fast and clinically applicable approach for designing the trabecular-like structure of tailored implants.

2. Materials and Methods

2.1. Design and fabrication of structures

In the present study, the mathematical equation of gyroid structure was converted to 3D CAD model using Rhinoceros 7 commercial software with Grasshopper plugin, and then with Autodesk Netfabb Ultimate 2021 software, it was modified and prepared for 3D printing. The theoretical equation of gyroid structure is as follows:

$$\cos(ax) \sin(by) + \cos(by) \sin(cz) + \cos(cz) \sin(ax) = 0 \quad (1)$$

This function is adapted from a review on equations for TPMS geometries by von Schnering and Nesper (Schnering and Nesper, 1991) and a combination of works presented in the literature (Feng et al, 2019; Yan et al., 2014; Yu et al., 2020; Barba et al., 2019). In this equation, a, b, and c are variables that determine the solid fraction (i.e. relative density of structure which equals to ratio of struts volume to total volume) and strut and cell size of the structure. Different views of a Gyroid unit cell are illustrated in Fig. 1. Here, five different gyroid TPMS structures with identical strut sizes of 300 μm and different solid fractions of 0.16, 0.26, 0.36 and 0.56 were designed. The dimension of the designed samples was selected to be 6×6×12 mm based on ISO13314 standard. As represented in Fig. 2, two groups of samples with solid fractions of 0.26 and 0.56 were manufactured in an argon gas atmosphere by an SLM machine (NOURA M100P) with optimized parameters, maximum laser power of 300W, and layer thickness of 30 μm . The Ti6Al4V powder used for this fabrication was gas atomized with a nearly spherical shape and particle size of less than 65 μm . The powder's elemental composition is reported in Table1. The building direction was in parallel with the Z axis of CAD models and 400-450 slices formed the final shapes (Fig. 2). At the end of fabrication, all

samples were removed from the platform by wire cutting machine and ultrasonically cleaned. In order to remove the unsintered powder, sandblasting post-processing was performed on all specimens.



Fig. 1. a) Gyroid unit cell architecture in front, b) top, and c) 3D views.

Table 1- Chemical Composition of Ti6Al4V powder used in this study

Element	Min. Wt%	Max. Wt%
Al	5.50	6.75
V	3.50	4.50
Fe	-	0.30
O	-	0.20
C	-	0.08
N	-	0.05
H	-	0.015
Y	-	0.005
Other elements each	-	0.10
Other elements total	-	0.40
Ti	Bal.	

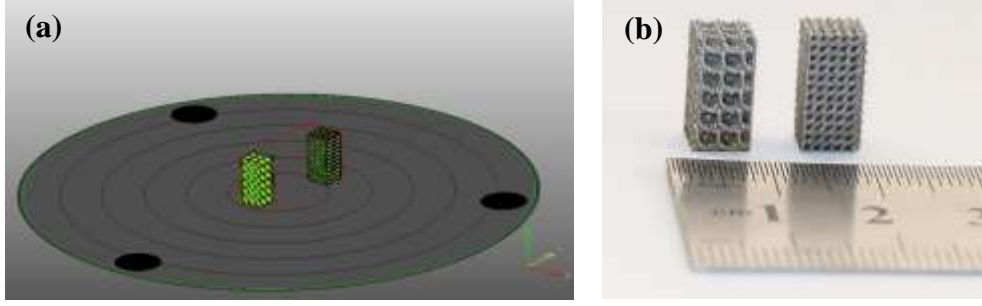


Fig. 2. a) The building orientation of samples in the manufacturing process and b) The manufactured samples.

2.2. Measurement and morphological characterization

In order to evaluate the manufacturability of designed lattices, a Micro-Computed tomography (Micro CT, LOTUS in Vivo) was utilized to scan the samples and characterize their 3D morphology. For this purpose, a 10 μm resolution Micro CT scanner was used at a tube voltage of 90 kV and tube current of 58 μA . Thereafter, 3D models were reconstructed using Avizo Lite 2019 software. The percent of solid and empty parts cannot be theoretically calculated unless we know the exact density of structures. Thus, the samples were immersed in alcohol for 2 hours and then their densities were obtained based on Archimedes' formula, which is the following equation (Carlos et al., 1998; Yáñez et al., 2018):

$$\rho_s = \left(\frac{\rho_{alc} * W_a}{W_a - W_{alc}} \right) \quad (2)$$

Where W_a and W_{alc} are the weights of the samples in air and alcohol respectively and ρ_{alc} is the density of alcohol (0.789 g/cm³). After determining the density, the relative density (solid fraction) was computed as follows (Carlos et al., 1998; Yáñez et al., 2018):

$$P_v = \left(\frac{\rho_s}{\rho_d} \right) \quad (3)$$

Where ρ_d is the theoretical bulk density of Ti6Al4V (4.42 g/cm³).

Concerning the microstructure examination of structures, an optical microscope (OM, Dino Eye. AM 423X) and for finer details SEM (VEGA3 TESCAN) were utilized. However, before any

microstructure observations, samples were cut, mounted, grounded by SiC papers (#500, #800, #1000, #1500, and #2000), polished with diamond paste, and etched for 35s in Kroll etchant solution (100 ml H₂O, 5 ml HNO₃ and 2.5 ml HF).

2.3. Permeability Measurement

Falling head method was used to measure the permeability of samples, and to ensure the accuracy of data for each structure three samples were evaluated. In the course of the experiment, as shown in Fig. 3, the sample was fixed at the end of the standpipe and then the standpipe was filled with water, next the time t_1 and t_2 were recorded at heights L_1 and L_2 , respectively, which were constant for all samples. Eventually, using Darcy's law which is the following equation, permeability (k) was examined:

$$k = \frac{K\mu}{\rho g} \quad (4)$$

Where μ is the dynamic viscosity coefficient of water, ρ is the density of water, g is gravity, and K is hydraulic conductivity which its formula is as below:

$$K = \frac{aH}{A(t_2 - t_1)} \ln\left(\frac{L_1}{L_2}\right) \quad (5)$$

Where “H” is the height of the samples, and “a” and “A” are the cross section area of the standpipe and samples respectively (Y. Li et al., 2019; Pennella et al., 2013).

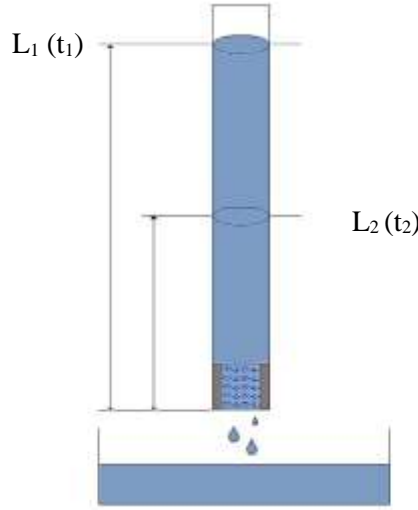


Fig. 3. Schematic of permeability measurement (Falling-Head method).

2.4. Mechanical Behavior Evaluation

The Finite Element Model (FEM) used for numerical analysis of designed structures was created using Abaqus/Explicit. For this purpose, 3D models were placed between two rigid plates. The rigid plate at the bottom of the sample was fixed and all its degrees of freedom were closed, and the plate at the top of the sample was movable and loaded along the Z axis at a constant speed. The vertical displacement was applied to the upper surface by half the length of the sample in such a way as to compress the specimen to 50% of its length. The applied boundary conditions are shown in Fig. 4. For finite element analysis, isotropic material properties were considered. Since it has been proven that the mechanical properties of additively manufactured materials are different from those that of conventionally produced, properties of additively manufactured Ti6Al4V alloy for this study were taken from the literature and inserted to Abaqus. For this purpose, an elastic modulus of 107 GPa and a Poisson's ratio of 0.3 were considered for the elastic properties (Wang and Li, 2018). The plastic deformation of Ti6Al4V is described by the Johnson–Cook plasticity model (Johnson and Cook, 1983), which accounts for strain rate, thermal softening, and strain hardening. According to the model, the flow stress in plastic region can be represented by the equation below:

$$\sigma_s = [A + B(\epsilon_e)^N] \cdot \left[1 + C \ln\left(\frac{\dot{\epsilon}^p}{\dot{\epsilon}^0}\right)\right] \cdot \left[1 - \left(\frac{T - T_{room}}{T_m - T_{room}}\right)^M\right] \quad (6)$$

where A, B, N, C, and M are constant values of material-related parameters according to the flow stress data, ϵ_e , $\dot{\epsilon}^p$ and $\dot{\epsilon}^0$ are the equivalent plastic strain, equivalent plastic strain rate, and the reference equivalent plastic strain rate, respectively. T_{room} is the room temperature, and T_m is the absolute melting temperature. The input parameters of Johnson-Cook model for Ti6Al4V were obtained from previous studies [31,33], as listed in Table 2.

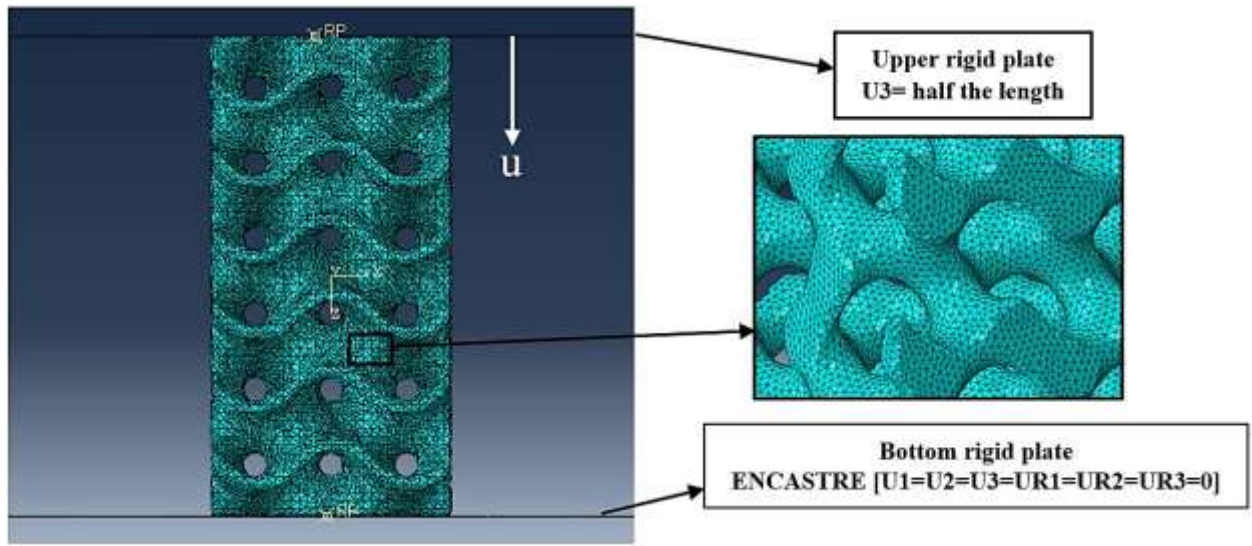


Fig. 4. Boundary conditions in simulation.

Table 2. Constitutive parameters of Johnson-Cook Plasticity model used in FEM.

A (MPa)	B (MPa)	N	C	M
1567	952	0.4	0	0

In order to compromise the simulated behavior of the lattice structures with their real conditions, two of samples with solid fractions of 0.26 and 0.56 were examined in the compression test. Based on ISO13314 Instruction, unidirectional compression tests were carried out on samples at room temperature with a

universal testing machine and with a strain rate of 0.5 mm/min. The load-displacement curve of each test was recorded and stress (σ), strain (ϵ), the elastic modulus (E), and yield strength (σ_y) were calculated, and the stress-strain curves were plotted.

3. Results and Discussion

3.1. Manufacturability

Fig. 5 compares the 3D models of samples from primary CAD file with their reconstructed ones by Micro-CT data besides their cross sections. It is noticeable that the samples were successfully and with a high dimensional accuracy built. Additionally, the SEM images from their top surfaces shown in Fig. 6 are in accordance with this matter. Table 3 represents the solid fraction and channel size of the samples obtained using Micro-CT data, density measurements, microscopic observations, and the CAD files. According to this table, the channel sizes in manufactured samples is slightly smaller than the designed values. In other words, the strut size became bigger after the manufacturing process (from 300 μm to approximately 315 μm). However, given the nature of the SLM process, such an observation was not far from expectation, and this relatively small difference can be ignored because in SLM procedure the molten pools become unstable due to the thermos-capillary flow (Gu et al., 2013; Lee et al., 1998; Ma et al., 2019b; Rombouts et al., 2006; Yadroitsev et al., 2007). This also explains the higher solid fraction after construction (see Table 3).

Microstructural characterization revealed the same type of microstructure for both groups of samples (Fig. 7). The α' phase with fine and orthogonally oriented martensitic laths is the only phase that can be observed. It is known that the formation of this phase is due to the rapid cooling rate during the SLM procedure as many of the previous β changes to the acicular α' martensitic (Eshawish et al., 2021; Fotovvati et al., 2012).

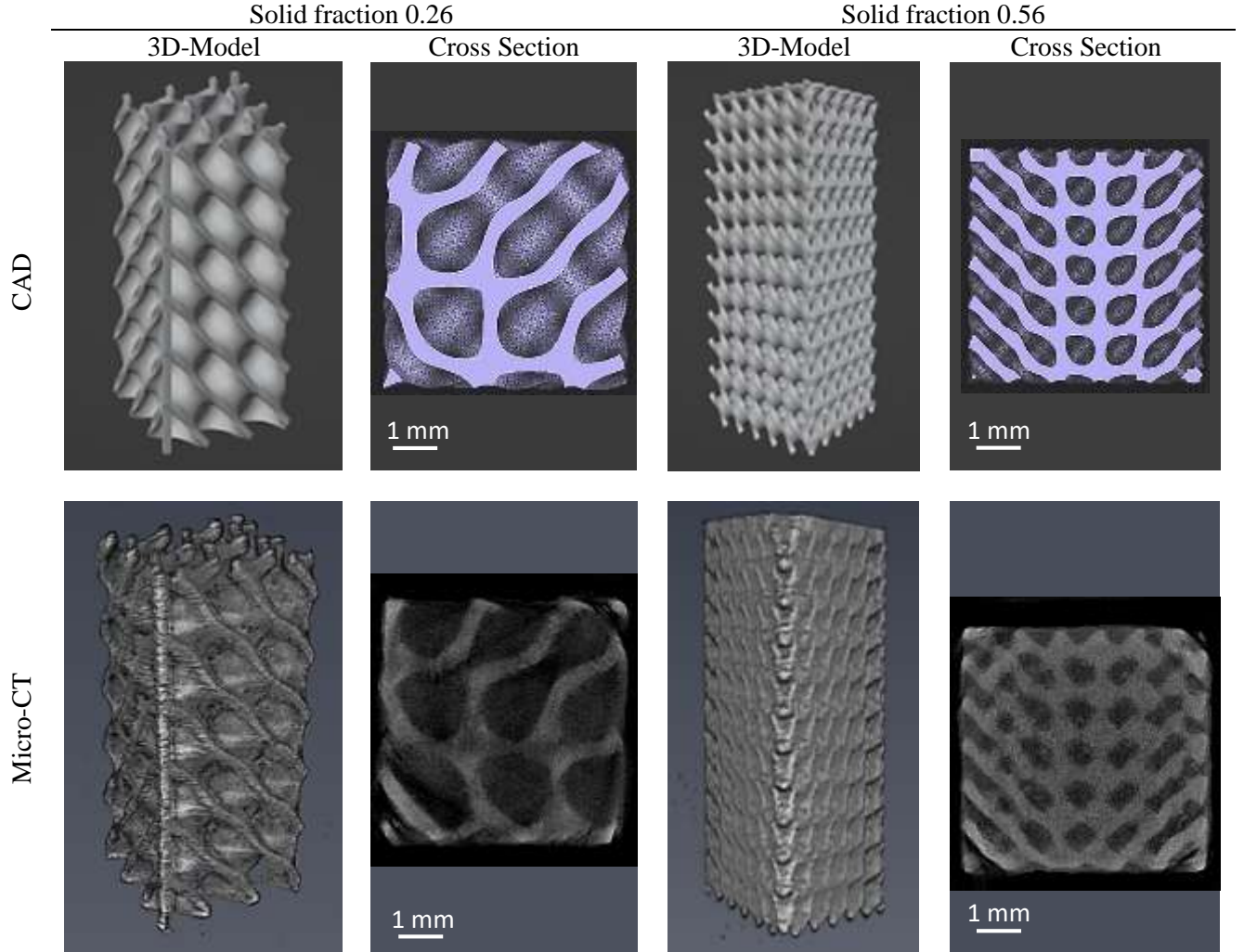


Fig. 5. 3D designs and cross-section of samples from both CAD and Micro-CT data.

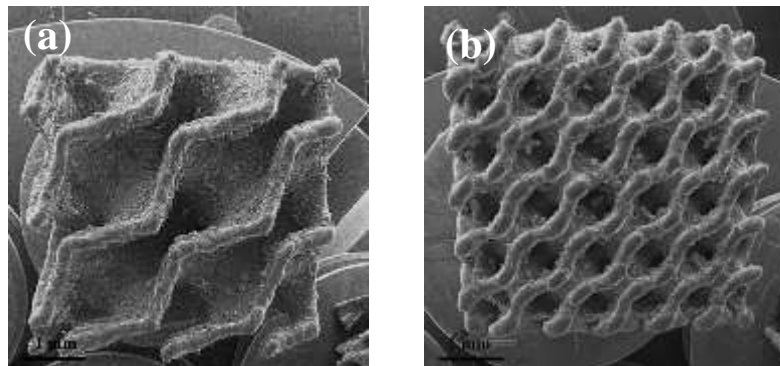


Fig. 6. SEM images from top surfaces of samples with solid fractions of a) 0.26 and b) 0.56

Table 3- Geometrical data obtained from the design and the computation.

Solid Fraction, %			Channel Size, μm		
Designed	Micro-CT	Density Measurements	Designed	Micro-CT	Microscopic Observations
26	29	31	1600	1510	1530
56	56	58	600	550	560

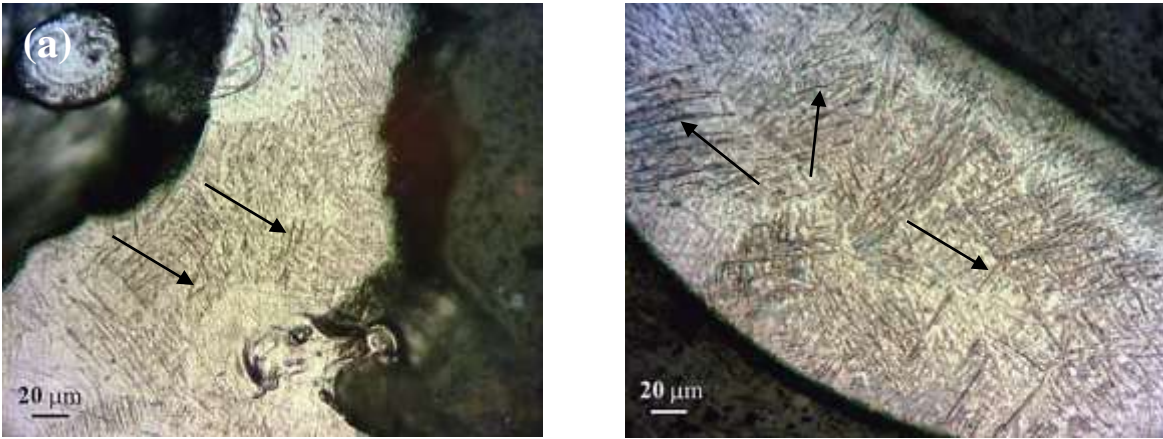


Fig. 7. OM images from etched surfaces of samples with solid fractions of a) 0.26 and b) 0.56. Typical acicular martensitic α' phases are indicated by arrows.

3.2. Permeability

Permeability is defined as a parameter to analyses lattices mass transport characteristics as they affect bone growth (Hollister, 2005; Sanz-Herrera et al., 2007; Jones et al., 2009; Mitsak et al., 2011). It quantitatively measures the capability of a porous structure to conduct fluid flow and depends on the combination of interconnectivity, solid fraction, channel size, orientation, and tortuosity. Furthermore, permeability impacts bone regeneration not only because higher values are proved to enhance bone ingrowth (Mitsak et al., 2011), but also because inadequate values may lead to the formation of cartilaginous instead of bone tissue (Kemppainen, 2008; Jeong et al., 2011). Values of permeability in the case of trabecular bone is depended on different conditions such as the anatomic site and the age of the person. For

instance, Nauman and coworkers (Nauman et al., 1999) found out that the permeability of the proximal femur is strongly greater than the vertebral body. Therefore, instead of a specific value, a range of permeabilities is found in the literature (1.00×10^{-11} to $1.21 \times 10^{-8} \text{ m}^2$). In the current study, the permeabilities of samples with solid fractions of 0.26 and 0.56 were found to be 0.38×10^{-9} and $0.16 \times 10^{-9} \text{ m}^2$, respectively. In both cases, the values are applicable and as is clear, the higher permeability of 0.26 solid fraction is due to its bigger channel size. A straight-through connecting structure would result in a higher permeability and the obstructive structure of the Gyroid against the fluid flow is the reason why the permeabilities of structures in this study are not in the greater-value part of the above-mentioned range.

3.3. Mechanical Properties

3.3.1. Compression Behavior

Fig. 8 shows the stress-strain curve from finite element analysis. The stress-strain curves start with a linear elastic behavior. The slope of the linear region shows the elastic modulus (stiffness) of each structure. At the end of the elastic zone, the highest peak on the curve can be seen, where the structures withstand the most stress and show the most strength. Then curves enter the plastic region, where with a slight increase in stress, a wide range of strain and deformation can be observed (Zhang et al., 2021). This trend with a wide plateau region makes the structures appropriate for high energy absorption applications. For solid fractions 0.36 and 0.56, the last part of the curves which shows a rise in stress is called densification, where the stress differs from being plateau and increases again. The reason for this rise in stress is that the struts of the structures come into contact with each other. Other samples have not experienced this step due to the lower solid fractions. Densification of these samples can be revealed in Figure 9. This figure illustrates the displacement and Von-Mises stress distributions of samples at different strains.

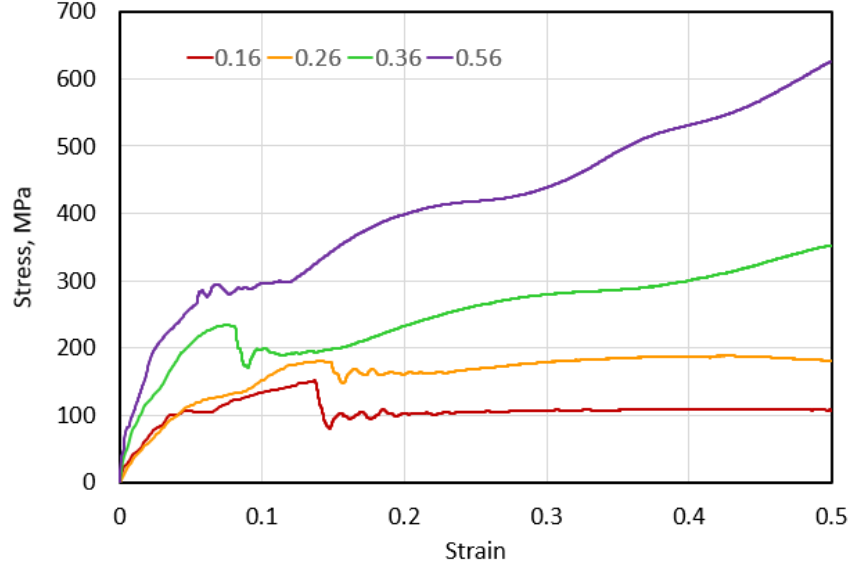


Fig. 8. Stress-strain curves from finite element analysis for different solid fractions.

Figure 10 shows the stress strain curves from uniaxial compression test for manufactured structures along with images of compressed samples. The stress-strain curves, relatively show good stability and have a similar trend to the curves from the finite element analysis. The fluctuations in plateau region indicate that the structure fails layer by layer. The obtained data from experiments besides the results of finite element analysis are given in Table 4. Similar to the finite element analysis results, the sample with a solid fraction of 0.56 shows a higher yield strength and stiffness in compression test. Indeed, with the increase of the solid fraction, the stiffness and yield strength of the structures increased. Designing the implant in a way that its stiffness is within the appropriate range (1.30 to 5.3 GPa for tibia, femur, and proximal bone (Gibson and Ashby, 2014)) can prevent the creation of stress shielding phenomena. As the table demonstrates, the elastic modulus of structures in this research is also within this range. Differences in experimental and numerical values can be justified by the discrepancy between the fabricated lattices geometry and the nominal CAD input, manufacturing imperfections, un-melted powders, and surface abnormalities (Wauthle et al. 2015; Dallago et al., 2018). However, an acceptable discrepancy of within 10% is found between the experimental and FEM results, which is in the same order as that outlined in the literature (Dallago et al., 2018).

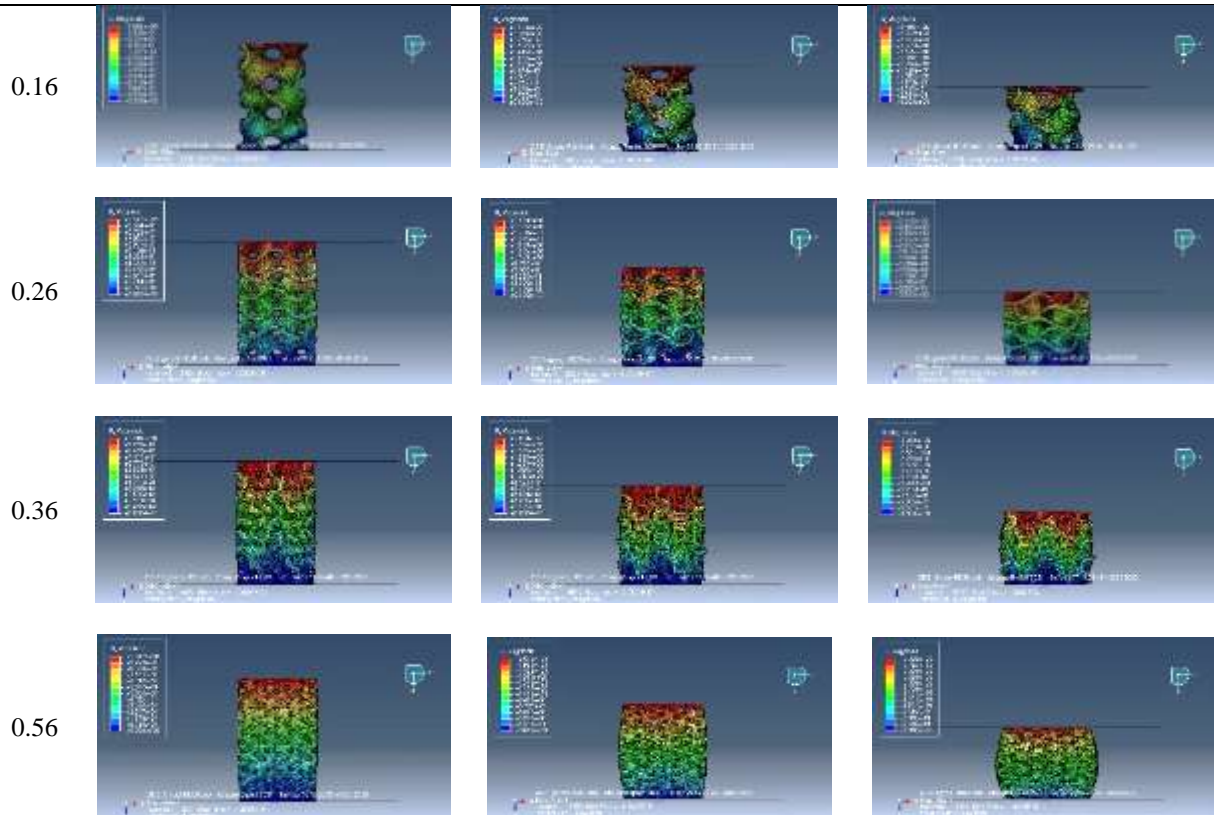
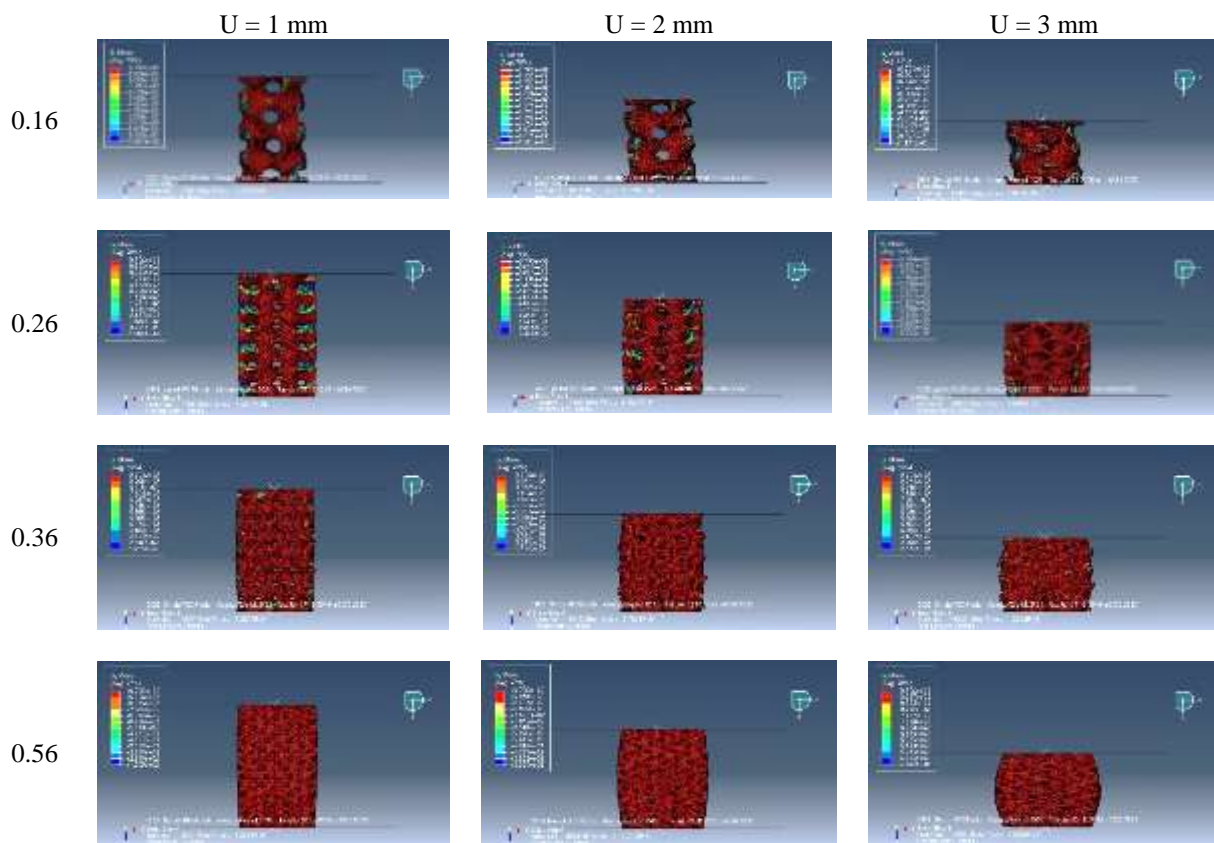


Fig. 9. Compressive deformation at different compressive strains, a) Von-Mises stress; and b) displacement distributions.

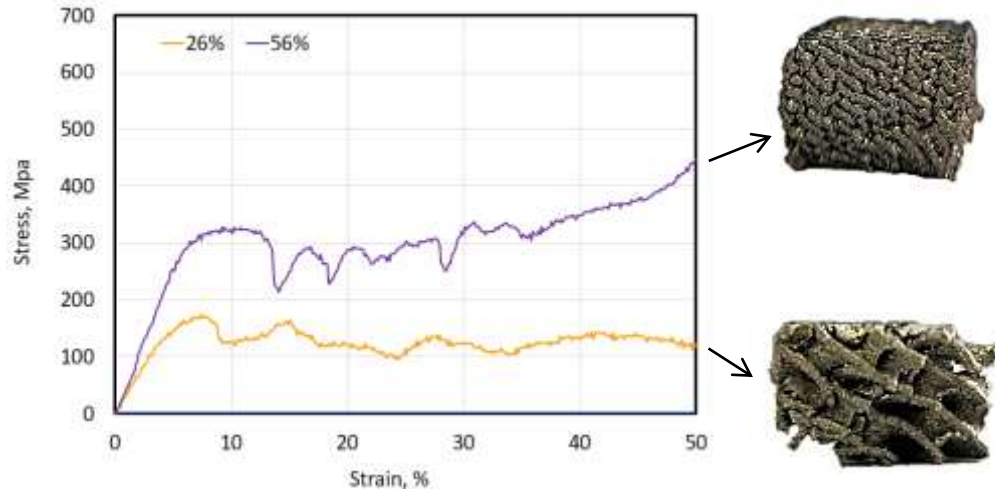


Fig. 10. Stress-strain curves from the compression test and compressed samples.

Table 4- The effect of relative density on the mechanical properties of structures

Solid Fraction	Stiffness, GPa			Yield Strength, MPa		
	Experiment	Simulation	% Error	Experiment	Simulation	% Error
0.16	-	1.08	-	-	147.02	-
0.26	2.41	2.23	-7.1	171.42	168.78	-1.5
0.36	-	3.07	-	-	232.24	-
0.56	4.63	4.47	-2.1	305.17	295.13	-3.3

3.3.2. Mechanical Properties and Solid Fraction Relations

The relationships between the mechanical properties of the lattice structures and their solid fraction (relative density) can be described using the exponential function presented by Gibson and Ashby (Gibson and Ashby, 2014):

$$E^* = C_1 \rho^n + E_0 \quad (7)$$

$$\sigma^* = C_2 \rho^m + \sigma_0 \quad (8)$$

where, ρ is the solid fraction or relative density of the structure, E_0 and σ_0 are the offset of the elastic modulus and yield strength, respectively, C_1, C_2, n and m are the material and structural constants. By depicting the changes in the mechanical properties of the structures based on their solid fractions in logarithmic scale, constant of equations (7) and (8) can be obtained (Fig. 11). These isolated equations can be applied in order to make customized design for implant much easier. Therefore, according to the desired strength and stiffness (based on the patient's age, gender, bone density, etc.), the appropriate and safe range of the implant's solid fraction can be selected with the help of the derived equation. Hence the process of designing personalized bespoke implants can be greatly facilitated.

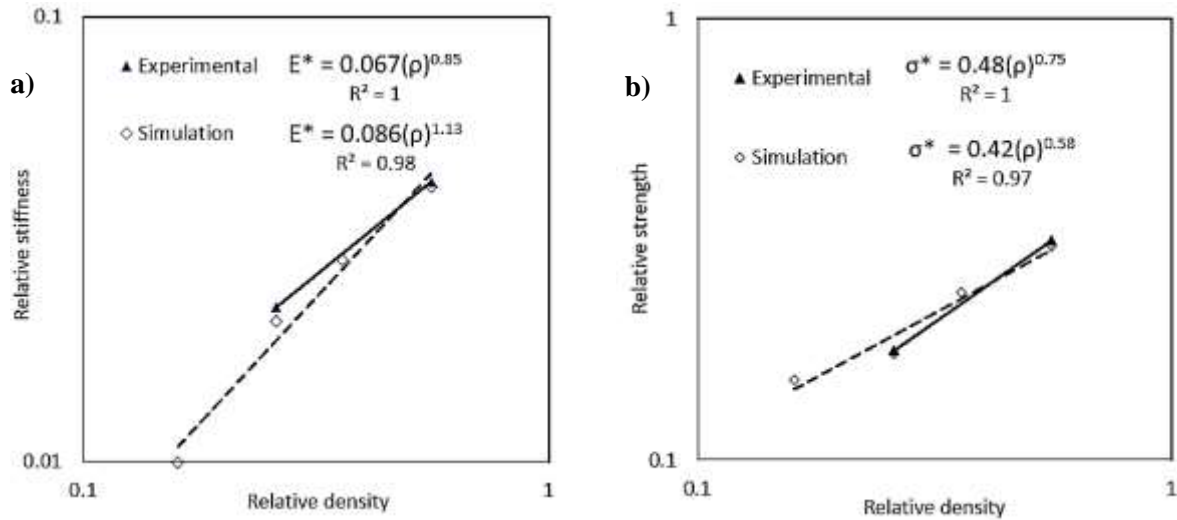


Fig. 11. Relationship between a) relative stiffness, and b) relative strength and solid fraction for implant design.

3.3.3. Energy Absorption Evaluation

The energy absorption capacity is a determining characteristic of lattice structures to evaluate their mechanical properties. Solid fraction or relative density is one of the most influencing parameters of cellular structures, and therefore, understanding the relationship between relative density and energy absorption properties is of great importance. The energy absorption (EA) of the structures during the compression test can be calculated as below by integrating the stress-strain curve (D. Li et al., 2019; Ma et al., 2021; Zhang et al., 2021):

$$W = \int_0^{\varepsilon_d} \sigma(\varepsilon) d\varepsilon \quad (9)$$

Where ε_d is the maximum strain at the onset of the densification stage. The densification strain (ε_d) is defined as the corresponding strain to the maximum energy absorption efficiency $\eta(\varepsilon)$, which can be written as follows (Li et al., 2006):

$$\eta(\varepsilon) = \frac{\int_0^{\varepsilon_0} \sigma(\varepsilon) d\varepsilon}{\sigma(\varepsilon_0)}, \frac{d\eta(\varepsilon)}{d\varepsilon} \Big|_{\varepsilon=\varepsilon_d} = 0 \quad (10)$$

Where $\sigma(\varepsilon_0)$ is the peak stress during the deformation up to the strain ε . In effect, the densification strain refers to the corresponding strain to the peak point of the energy absorption efficiency curve. Specific energy absorption (SEA) which is shown in equation 11 is the most common method used to reveal the energy absorption capability (D. Li et al., 2019; Ma et al., 2021; Zhang et al., 2021):

$$SEA = \frac{\int_0^{\varepsilon_d} \sigma(\varepsilon) d\varepsilon}{\rho} \quad (11)$$

Where ρ is the relative density of structure. The relation between the energy absorption and the specific energy absorption value of structures and strain values for different solid fractions are presented in Fig. 12. In addition, the experimental and numerical value of energy absorptions efficacy of the samples are listed in Table 5. It can be clearly seen that the energy absorption capacity of structures enhances with the increase of relative density. Additionally, the results obtained from both methods show an acceptable similarity.

Although, energy absorption capacity of designed structures increased with solid fraction, the specific energy absorption of samples is in the same range, which indicates the identical energy absorption properties of samples due to their analogous structure. However, calculated energy absorption efficacy values from experimental and FEM results reveal that the values of sample with solid fraction of 0.26 is the highest. This is attributed to the compression behavior of this sample, in which the stress-strain curve exhibits less fluctuations. The smoother stress strain curve besides the higher densification strain in samples with lower solid fractions leads them to absorb more energy at the same stress. Furthermore, it is found that when the solid fraction is increased from 0.26 to 0.56 mm, the energy absorption efficiency of the structures is remarkably reduced by about 26%. This is because of higher densification strain of the sample with solid fraction of 0.56. In summary, energy absorption capacity of structures increases with increasing the solid fraction. Besides, all structures show relatively the similar energy abortion behavior, the structures with lower solid fractions have higher values of energy absorption efficacy.

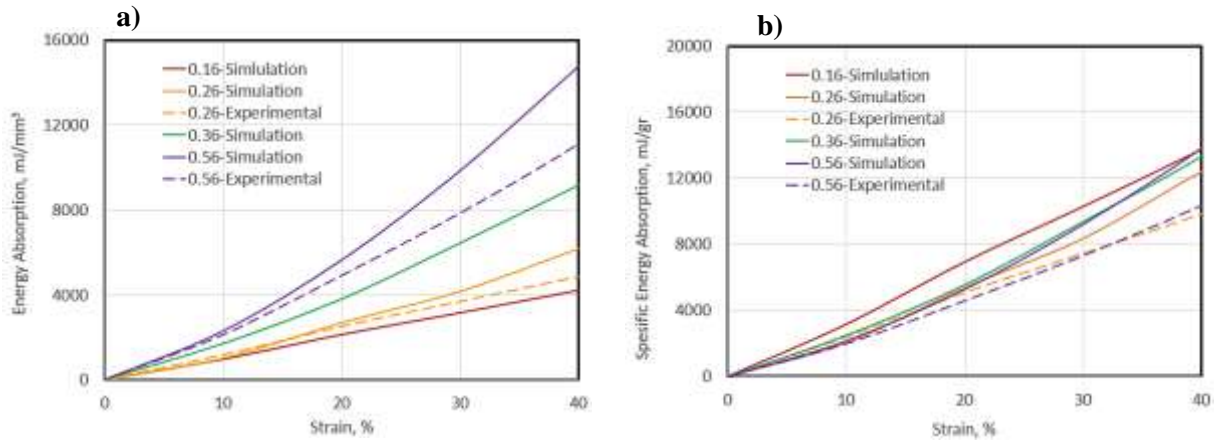


Fig. 12. a) The energy absorption and b) the specific energy absorption of structures versus strain.

Table 5. Energy absorption efficacy values obtained from compression test and FEM.

Solid Fraction, %	Energy Absorption Efficacy, %		
	Experiment	Simulation	% Error
16	-	72.38	-
26	76.46	80.44	5.2
36	-	64.67	-
56	58.19	54.12	-7.0

4. Conclusion

This research was carried out to find an isolated relation between the Gyroid lattice structure's solid fraction and its mechanical properties of strength, stiffness, and energy absorption. These relations can greatly enhance the design of custom trabecular bone implants. By considering the tibia component in the knee joint replacements, different Gyroid structures with solid fractions of 16%, 26%, 36% and 56% were designed and with the help of finite element analysis, the mentioned relations were found. Moreover, with the help of the SLM machine two of them with solid fractions of 26% and 56% were manufactured to evaluate their manufacturability and permeability and to ensure the accuracy of the simulation results. The main results were as follows:

- 1- The Ti6Al4V lattices with gyroid structures fabricated employing SLM presented stable manufacturability, which was demonstrated by the accuracy of the solid fractions and the manufacturing deviation of the struts and channels size.
- 2- The permeability behavior of the gyroid structures was evaluated through experimental method. The permeability of manufactured samples ranged from 0.38×10^{-9} and $0.16 \times 10^{-9} \text{ m}^2$, which was in the range of tibia bone, and their permeabilities decreased as solid fraction increased. Even though,

the straight-thorough connecting structure of the Gyroid structure showed an obstructive behavior against fluid flow.

- 3- FEM and experimental assessment of compression behavior of the Ti6Al4V gyroid lattices manufactured by SLM showed that the structures can have adjustable mechanical properties. The structures can reduce the implant stiffness to the same range of trabecular bone stiffness. The stiffness and yield strengths of the gyroid lattices ranged from 1.08 to 4.47 GPa and 147 to 295 MPa, respectively, which satisfy the requirements of natural trabecular bones. Indeed, the designed structures can match the stiffness of human bone with the change of solid fraction. Hence, they can reduce the probability of stress shielding phenomenon and implant failure. Also, their high mechanical strength prevents implant failure under mechanical loading.
- 4- The obtained relationships from mechanical behavior assessment can be used to choose the solid fraction of the structure within a safe range by considering the strength and stiffness of the desired bone (according to the age and bone density of the patient) in the process of implant design. Consequently, it makes implant personalization fast and simple.
- 5- The energy absorption capability of the structures was improved by increasing the relative density. In terms of specific energy absorption, all structures exhibited relatively same values due to their identical lattice structure. Moreover, the structure with 26% solid fraction exhibited the highest value of energy absorption efficacy which was associated to its smoother stress-strain curve and high densification strain. In effect, energy absorption evaluations demonstrated that the samples with lower solid fractions are capable of absorb more energy at the same stress compared with samples with higher solid fractions.

Statements and Declarations

Competing Interests and Funding

The authors report there are no competing interests to declare.

This work was supported by the Shiraz University; and the Mehrawin Shiraz Co.

5. References

- Aufa, A.N., Hassan, M.Z., Ismail, Z., 2022. Recent advances in Ti-6Al-4V additively manufactured by selective laser melting for biomedical implants: Prospect development. *Journal of Alloys and Compounds* 896, 163072.
<https://doi.org/10.1016/J.JALLCOM.2021.163072>
- Barba, D., Alabort, E., Reed, R.C., 2019. Synthetic bone: Design by additive manufacturing. *Acta Biomaterialia* 97, 637–656. <https://doi.org/10.1016/J.ACTBIO.2019.07.049>
- Benedetti, M., du Plessis, A., Ritchie, R.O., Dallago, M., Razavi, S.M.J., Berto, F., 2021. Architected cellular materials: A review on their mechanical properties towards fatigue-tolerant design and fabrication. *Materials Science and Engineering: R: Reports* 144, 100606.
<https://doi.org/10.1016/J.MSER.2021.100606>
- Bertol, L.S., Júnior, W.K., Silva, F.P. da, Aumund-Kopp, C., 2010. Medical design: Direct metal laser sintering of Ti–6Al–4V. *Materials & Design* 31, 3982–3988.
<https://doi.org/10.1016/J.MATDES.2010.02.050>
- Bidan, C.M., Wang, F.M., Dunlop, J.W.C., 2013. A three-dimensional model for tissue deposition on complex surfaces. <https://doi.org/10.1080/10255842.2013.774384> 16, 1056–1070. <https://doi.org/10.1080/10255842.2013.774384>
- Bobbert, F.S.L., Lietaert, K., Eftekhari, A.A., Pouran, B., Ahmadi, S.M., Weinans, H., Zadpoor, A.A., 2017. Additively manufactured metallic porous biomaterials based on minimal surfaces: A unique combination of topological, mechanical, and mass transport properties. *Acta biomaterialia* 53, 572–584. <https://doi.org/10.1016/J.ACTBIO.2017.02.024>

- Dallago, M., Fontanari, V., Torresani, E., Leoni, M., Pederzoli, C., Potrich, C., & Benedetti, M. (2018). Fatigue and biological properties of Ti-6Al-4V ELI cellular structures with variously arranged cubic cells made by selective laser melting. In *Journal of the Mechanical Behavior of Biomedical Materials* (Vol. 78, pp. 381–394).
<https://doi.org/10.1016/j.jmbbm.2017.11.044>
- Dhiman, S., Joshi, R.S., Singh, S., Gill, S.S., Singh, H., Kumar, R., Kumar, V., 2021. A framework for effective and clean conversion of machining waste into metal powder feedstock for additive manufacturing. *Cleaner Engineering and Technology* 4, 100151.
<https://doi.org/10.1016/J.CLET.2021.100151>
- Dhiman, S., Sidhu, S.S., Bains, P.S., Bahraminasab, M., 2019. Mechanobiological assessment of Ti-6Al-4V fabricated via selective laser melting technique: a review. *Rapid Prototyping Journal* 25, 1266–1284. <https://doi.org/10.1108/RPJ-03-2019-0057/FULL/XML>
- Eshawish, N., Malinov, S., Sha, W., Walls, P., 2021. Microstructure and Mechanical Properties of Ti-6Al-4V Manufactured by Selective Laser Melting after Stress Relieving, Hot Isostatic Pressing Treatment, and Post-Heat Treatment. *Journal of Materials Engineering and Performance* 30, 5290–5296. <https://doi.org/10.1007/S11665-021-05753-W>
- Feng, J., Fu, J., Lin, Z., Shang, C., & Niu, X. (2019). Layered infill area generation from triply periodic minimal surfaces for additive manufacturing. In *CAD Computer Aided Design* (Vol. 107, pp. 50–63). <https://doi.org/10.1016/j.cad.2018.09.005>
- Fotovvati, B., Namdari, N., Dehghanghadikolaei -, A., Dai, N., Zhang, J., Chen, Y., -, al, Liu, W., Liu -, Z., Simonelli, M., Tse, Y.Y., Tuck, C., 2012. Microstructure of Ti-6Al-4V produced by selective laser melting. *Journal of Physics: Conference Series* 371, 012084.

<https://doi.org/10.1088/1742-6596/371/1/012084>

Geetha, M., Singh, A.K., Asokamani, R., Gogia, A.K., 2009. Ti based biomaterials, the ultimate choice for orthopaedic implants – A review. *Progress in Materials Science* 54, 397–425.

<https://doi.org/10.1016/J.PMATSCI.2008.06.004>

Gibson, L.J., Ashby, M.F., 2014. *Cellular solids: Structure and properties*, second edition.

Cellular Solids: Structure and Properties, Second Edition 1–510.

<https://doi.org/10.1017/CBO9781139878326>

Gu, D.D., Meiners, W., Wissenbach, K., Poprawe, R., 2013. Laser additive manufacturing of metallic components: materials, processes and mechanisms.

<https://doi.org/10.1179/1743280411Y.0000000014> 57, 133–164.

<https://doi.org/10.1179/1743280411Y.0000000014>

Hollister, S. J. (2005). Porous scaffold design for tissue engineering. In *Nature Materials* (Vol. 4, Issue 7, pp. 518–524). <https://doi.org/10.1038/nmat1421>

Hsieh, M.T., Begley, M.R., Valdevit, L., 2021. Architected implant designs for long bones: Advantages of minimal surface-based topologies. *Materials & Design* 207, 109838.

<https://doi.org/10.1016/J.MATDES.2021.109838>

Jeong, C. G., Zhang, H., & Hollister, S. J. (2011). Three-dimensional poly(1,8-octanediol-co-citrate) scaffold pore shape and permeability effects on sub-cutaneous in vivo chondrogenesis using primary chondrocytes. In *Acta Biomaterialia* (Vol. 7, Issue 2, pp. 505–514). <https://doi.org/10.1016/j.actbio.2010.08.027>

Jinnai, H., Watashiba, H., Kajihara, T., Nishikawa, Y., Takahashi, M., Ito, M., 2002. Surface

curvatures of trabecular bone microarchitecture. *Bone* 30, 191–194.

[https://doi.org/10.1016/S8756-3282\(01\)00672-X](https://doi.org/10.1016/S8756-3282(01)00672-X)

Johnson, G. R., & Cook, W. H. (1983). A Computational Constitutive Model and Data for Metals Subjected to Large Strain, High Strain Rates and High Pressures. The Seventh International Symposium on Ballistics, 541–547.

Jones, A. C., Arns, C. H., Hutmacher, D. W., Milthorpe, B. K., Sheppard, A. P., & Knackstedt, M. A. (2009). The correlation of pore morphology, interconnectivity and physical properties of 3D ceramic scaffolds with bone ingrowth. In *Biomaterials* (Vol. 30, Issue 7, pp. 1440–1451). <https://doi.org/10.1016/j.biomaterials.2008.10.056>

Katz, J.L., 1980. Anisotropy of Young's modulus of bone. *Nature* 1980 283:5742 283, 106–107. <https://doi.org/10.1038/283106a0>

Kemppainen, J. (2008). Mechanically stable solid freeform fabricated scaffolds with permeability optimized for cartilage tissue engineering (p. 177). <http://proquest.umi.com.proxy.lib.umich.edu/pqdweb?did=1663913111&Fmt=7&clientId=17822&RQT=309&VName=PQD>

Krishna, B.V., Bose, S., Bandyopadhyay, A., 2007. Low stiffness porous Ti structures for load-bearing implants. *Acta biomaterialia* 3, 997–1006. <https://doi.org/10.1016/J.ACTBIO.2007.03.008>

Lee, P.D., Quested, P.N., McLean, M., 1998. Modelling of Marangoni effects in electron beam melting. *Philosophical Transactions of the Royal Society A: Mathematical, Physical and Engineering Sciences* 356, 1027–1043. <https://doi.org/10.1098/RSTA.1998.0207>

Léon Y León, C. A. (1998). New perspectives in mercury porosimetry. In *Advances in Colloid and Interface Science* (Vols. 76–77, pp. 341–372). [https://doi.org/10.1016/S0001-8686\(98\)00052-9](https://doi.org/10.1016/S0001-8686(98)00052-9)

Li, D., Liao, W., Dai, N., Xie, Y.M., 2019. Comparison of Mechanical Properties and Energy Absorption of Sheet-Based and Strut-Based Gyroid Cellular Structures with Graded Densities. *Materials* 12. <https://doi.org/10.3390/MA12132183>

Li, Q. M., Magkiriadis, I., & Harrigan, J. J. (2006). Compressive strain at the onset of densification of cellular solids. In *Journal of Cellular Plastics* (Vol. 42, Issue 5, pp. 371–392). <https://doi.org/10.1177/0021955X06063519>

Li, Y., Jahr, H., Pavanram, P., Bobbert, F.S.L., Puggi, U., Zhang, X.Y., Pouran, B., Leeftang, M.A., Weinans, H., Zhou, J., Zadpoor, A.A., 2019. Additively manufactured functionally graded biodegradable porous iron. *Acta Biomaterialia* 96, 646–661. <https://doi.org/10.1016/J.ACTBIO.2019.07.013>

Liu, F., Ran, Q., Zhao, M., Zhang, T., Zhang, D.Z., Su, Z., 2020. Additively Manufactured Continuous Cell-Size Gradient Porous Scaffolds: Pore Characteristics, Mechanical Properties and Biological Responses In Vitro. *Materials* (Basel, Switzerland) 13. <https://doi.org/10.3390/MA13112589>

Ma, S., Tang, Q., Feng, Q., Song, J., Han, X., Guo, F., 2019a. Mechanical behaviours and mass transport properties of bone-mimicking scaffolds consisted of gyroid structures manufactured using selective laser melting. *Journal of the Mechanical Behavior of Biomedical Materials* 93, 158–169. <https://doi.org/10.1016/J.JMBBM.2019.01.023>

Ma, S., Tang, Q., Feng, Q., Song, J., Han, X., Guo, F., 2019b. Mechanical behaviours and mass

- transport properties of bone-mimicking scaffolds consisted of gyroid structures manufactured using selective laser melting. *Journal of the mechanical behavior of biomedical materials* 93, 158–169. <https://doi.org/10.1016/J.JMBBM.2019.01.023>
- Ma, X., Zhang, D.Z., Zhao, M., Jiang, J., Luo, F., Zhou, H., 2021. Mechanical and energy absorption properties of functionally graded lattice structures based on minimal curved surfaces. *International Journal of Advanced Manufacturing Technology* 118, 995–1008. <https://doi.org/10.1007/S00170-021-07768-Y>
- Mitsak, A. G., Kemppainen, J. M., Harris, M. T., & Hollister, S. J. (2011). Effect of polycaprolactone scaffold permeability on bone regeneration in vivo. In *Tissue Engineering - Part A* (Vol. 17, Issues 13–14, pp. 1831–1839). <https://doi.org/10.1089/ten.tea.2010.0560>
- Mullen, L., Stamp, R.C., Brooks, W.K., Jones, E., Sutcliffe, C.J., 2009. Selective Laser Melting: a regular unit cell approach for the manufacture of porous, titanium, bone in-growth constructs, suitable for orthopedic applications. *Journal of biomedical materials research. Part B, Applied biomaterials* 89, 325–334. <https://doi.org/10.1002/JBM.B.31219>
- Nauman, E.A., Fong, K.E., Keaveny, T.M., 1999. Dependence of Intertrabecular Permeability on Flow Direction and Anatomic Site. *Annals of Biomedical Engineering* 27:4 27, 517–524. <https://doi.org/10.1114/1.195>
- Pennella, F., Cerino, G., Massai, D., Gallo, D., Falvo D’Urso Labate, G., Schiavi, A., Deriu, M.A., Audenino, A., Morbiducci, U., 2013. A survey of methods for the evaluation of tissue engineering scaffold permeability. *Annals of biomedical engineering* 41, 2027–2041. <https://doi.org/10.1007/S10439-013-0815-5>
- Rombouts, M., Kruth, J.P., Froyen, L., Mercelis, P., 2006. Fundamentals of selective laser

melting of alloyed steel powders. *CIRP Annals - Manufacturing Technology* 55, 187–192.

[https://doi.org/10.1016/S0007-8506\(07\)60395-3](https://doi.org/10.1016/S0007-8506(07)60395-3)

Sanz-Herrera, J. A., Garcia-Aznar, J. M., & Doblare, M. (2008). A mathematical model for bone tissue regeneration inside a specific type of scaffold. In *Biomechanics and Modeling in Mechanobiology* (Vol. 7, Issue 5, pp. 355–366). <https://doi.org/10.1007/s10237-007-0089-7>

Shah, F.A., Trobos, M., Thomsen, P., Palmquist, A., 2016. Commercially pure titanium (cp-Ti) versus titanium alloy (Ti6Al4V) materials as bone anchored implants — Is one truly better than the other? *Materials Science and Engineering: C* 62, 960–966.

<https://doi.org/10.1016/J.MSEC.2016.01.032>

Singh, M., Dhiman, S., Singh, H., Berndt, C.C., 2020. Optimization of modulation-assisted drilling of Ti-6Al-4V aerospace alloy via response surface method.

<https://doi.org/10.1080/10426914.2020.1772487> 35, 1313–1329.

<https://doi.org/10.1080/10426914.2020.1772487>

Singla, A.K., Banerjee, M., Sharma, A., Singh, J., Bansal, A., Gupta, M.K., Khanna, N., Shahi, A.S., Goyal, D.K., 2021. Selective laser melting of Ti6Al4V alloy: Process parameters, defects and post-treatments. *Journal of Manufacturing Processes* 64, 161–187.

<https://doi.org/10.1016/J.JMAPRO.2021.01.009>

The relationship between stress shielding and bone resorption around total hip stems and the effects of flexible materials - PubMed [WWW Document], n.d. URL

<https://pubmed.ncbi.nlm.nih.gov/1728998/> (accessed 9.24.22).

Titanium as the material of choice for cementless femoral components in total hip arthroplasty -

PubMed [WWW Document], n.d. URL <https://pubmed.ncbi.nlm.nih.gov/7634595/>

(accessed 11.13.22).

Topological Similarity of Sponge-like Bicontinuous Morphologies Differing in Length Scale -

Jinnai - 2002 - Advanced Materials - Wiley Online Library [WWW Document], n.d. URL

[https://onlinelibrary.wiley.com/doi/abs/10.1002/1521-](https://onlinelibrary.wiley.com/doi/abs/10.1002/1521-4095%2820021118%2914%3A22%3C1615%3A%3AAID-ADMA1615%3E3.0.CO%3B2-S)

[4095%2820021118%2914%3A22%3C1615%3A%3AAID-ADMA1615%3E3.0.CO%3B2-](https://onlinelibrary.wiley.com/doi/abs/10.1002/1521-4095%2820021118%2914%3A22%3C1615%3A%3AAID-ADMA1615%3E3.0.CO%3B2-S)

[S](https://onlinelibrary.wiley.com/doi/abs/10.1002/1521-4095%2820021118%2914%3A22%3C1615%3A%3AAID-ADMA1615%3E3.0.CO%3B2-S) (accessed 9.24.22).

van Blitterswijk, C.A., Grote, J.J., Kuijpers, W., Daems, W.T., de Groot, K., 1986. Macropore

tissue ingrowth: a quantitative and qualitative study on hydroxyapatite ceramic.

Biomaterials 7, 137–143. [https://doi.org/10.1016/0142-9612\(86\)90071-2](https://doi.org/10.1016/0142-9612(86)90071-2)

von Schnering, H. G., & Nesper, R. (1991). Nodal surfaces of Fourier series: Fundamental

invariants of structured matter. In Zeitschrift für Physik B Condensed Matter (Vol. 83, Issue

3, pp. 407–412). <https://doi.org/10.1007/BF01313411>

Voxelised Minimal Surface Structures (from Kapfer et al, Biomaterials 2011) – Gerd Schröder-

Turk [WWW Document], n.d. URL [https://gerdschroeder-turk.org/2012/02/21/voxelised-](https://gerdschroeder-turk.org/2012/02/21/voxelised-bone-scaffold-structures-used-in-kapfer-et-al-biomaterials-2011/)

[bone-scaffold-structures-used-in-kapfer-et-al-biomaterials-2011/](https://gerdschroeder-turk.org/2012/02/21/voxelised-bone-scaffold-structures-used-in-kapfer-et-al-biomaterials-2011/) (accessed 9.24.22).

Wang, Z., & Li, P. (2018). Characterisation and constitutive model of tensile properties of

selective laser melted Ti-6Al-4V struts for microlattice structures. In Materials Science and

Engineering A (Vol. 725, pp. 350–358). <https://doi.org/10.1016/j.msea.2018.04.006>

Wauthle, R., Vrancken, B., Beynaerts, B., Jorissen, K., Schrooten, J., Kruth, J. P., & Van

Humbeeck, J. (2015). Effects of build orientation and heat treatment on the microstructure

and mechanical properties of selective laser melted Ti6Al4V lattice structures. In Additive

Manufacturing (Vol. 5, pp. 77–84). <https://doi.org/10.1016/j.addma.2014.12.008>

- Yadroitsev, I., Bertrand, P., Smurov, I., 2007. Parametric analysis of the selective laser melting process. *Applied Surface Science* 253, 8064–8069.
<https://doi.org/10.1016/J.APSUSC.2007.02.088>
- Yan, C., Hao, L., Hussein, A., Young, P., Raymont, D., 2014. Advanced lightweight 316L stainless steel cellular lattice structures fabricated via selective laser melting. *Materials & Design* 55, 533–541. <https://doi.org/10.1016/J.MATDES.2013.10.027>
- Yáñez, A., Cuadrado, A., Martel, O., Afonso, H., & Monopoli, D. (2018). Gyroid porous titanium structures: A versatile solution to be used as scaffolds in bone defect reconstruction. In *Materials and Design* (Vol. 140, pp. 21–29).
<https://doi.org/10.1016/j.matdes.2017.11.050>
- Yu, G., Li, Z., Li, S., Zhang, Q., Hua, Y., Liu, H., Zhao, X., Dhaidhai, D.T., Li, W., Wang, X., 2020. The select of internal architecture for porous Ti alloy scaffold: A compromise between mechanical properties and permeability. *Materials & Design* 192, 108754.
<https://doi.org/10.1016/J.MATDES.2020.108754>
- Yuan, L., Ding, S., Wen, C., 2019. Additive manufacturing technology for porous metal implant applications and triple minimal surface structures: A review. *Bioactive Materials* 4, 56–70.
<https://doi.org/10.1016/J.BIOACTMAT.2018.12.003>
- Zhang, X. chun, Liu, N. nan, An, C. chao, Wu, H. xiang, Li, N., Hao, K. ming, 2021. Dynamic crushing behaviors and enhanced energy absorption of bio-inspired hierarchical honeycombs with different topologies. *Defence Technology*.
<https://doi.org/10.1016/J.DT.2021.11.013>